p-GaInP_2/TiO_2 exhibit oscillations similar to that for p-GaInP_2/Pt, meaning that the surface field increases substantially when the TiO_2 thickness increases from 0.5 to 35 nm. The formation and decay time constant of ΔF for these samples are extracted from the corresponding TPR kinetics (fig. S9B). Best-fit parameters are tabulated in table S1. Thicker TiO_2 layers exhibit slightly faster field formation but slower decay, which is likely due to the larger built-in field that drives carriers apart and separates them at a greater distance, both of which lead to slower recombination. We find that the kinetics are effectively unperturbed once a sufficient amorphous TiO_2 thickness has been reached, suggesting that thicker layers would not drastically influence the photoconversion performance from a charge dynamics perspective. A thick TiO_2 layer may still be necessary for other reasons (such as elimination of pinholes) that affect stabilization against photocorrosion, as has been found for 140-nm-thick amorphous TiO_2 layers on Si, GaAs, and GaP photoanodes (*2*).

Our results uncover key beneficial roles of amorphous TiO_2 in the energy-conversion process that have come under intense investigation after several recent reports of TiO_2-stablized photoelectrodes (*2*, *29*, *30*). The TPR technique developed here furthermore introduces a general method to understand charge transfer at semiconductor junctions.

REFERENCES AND NOTES

1. A. Fujishima, K. Honda, *Nature* **238**, 37–38 (1972).
2. S. Hu *et al.*, *Science* **344**, 1005–1009 (2014).
3. O. Khaselev, J. A. Turner, *Science* **280**, 425–427 (1998).
4. M. Grätzel, *Nature* **414**, 338–344 (2001).
5. N. S. Lewis, D. G. Nocera, *Proc. Natl. Acad. Sci. U.S.A.* **103**, 15729–15735 (2006).
6. M. C. Beard, G. M. Turner, C. A. Schmuttenmaer, *J. Phys. Chem. B* **106**, 7146–7159 (2002).
7. R. Ulbricht, E. Hendry, J. Shan, T. F. Heinz, M. Bonn, *Rev. Mod. Phys.* **83**, 543–586 (2011).
8. J. Shah, *Ultrafast Spectroscopy of Semiconductors and Semiconductor Nanostructures* (Springer, Berlin and Heidelberg, ed. 2, 1999).
9. Y. Yang, T. Lian, *Coord. Chem. Rev.* **263-264**, 229–238 (2014).
10. K. Tvrdy, P. A. Frantsuzov, P. V. Kamat, *Proc. Natl. Acad. Sci. U.S.A.* **108**, 29–34 (2011).
11. K. E. Knowles, M. D. Peterson, M. R. McPhail, E. A. Weiss, *J. Phys. Chem. C* **117**, 10229–10243 (2013).
12. V. I. Klimov, *Annu. Rev. Phys. Chem.* **58**, 635–673 (2007).
13. W. A. Tisdale *et al.*, *Science* **328**, 1543–1547 (2010).
14. Z. Chen *et al.*, *J. Mater. Res.* **25**, 3–16 (2010).
15. B. R. Bennett, R. A. Soref, J. A. del Alamo, *IEEE J. Quantum Electron.* **26**, 113–122 (1990).
16. D. E. Aspnes, *Phys. Rev. Lett.* **28**, 168–171 (1972).
17. S. Marcinkevičius *et al.*, *AIP Adv* **2**, 042148 (2012).
18. P. Emanuelsson *et al.*, *Appl. Phys. Lett.* **64**, 2849–2851 (1994).
19. K. L. Vodopyanov, H. Graener, C. C. Phillips, T. J. Tate, *Phys. Rev. B* **46**, 13194–13200 (1992).
20. A. J. Sabbah, D. M. Riffe, *J. Appl. Phys.* **88**, 6954–6956 (2000).
21. Y. Yang *et al.*, *Nat. Commun.* **6**, 7961 (2015).
22. H. Shen, M. Dutta, *J. Appl. Phys.* **78**, 2151–2176 (1995).
23. T. Kippenberg *et al.*, *Phys. Rev. B* **60**, 4446–4449 (1999).
24. F. H. Pollak, *Surf. Interface Anal.* **31**, 938–953 (2001).
25. H. Shen, F. H. Pollak, *Phys. Rev. B* **42**, 7097–7102 (1990).
26. T. Kita *et al.*, *J. Appl. Phys.* **94**, 6487–6490 (2003).
27. Y. S. Huang *et al.*, *Appl. Phys. Lett.* **73**, 214–216 (1998).
28. F. J. Schultes *et al.*, *Appl. Phys. Lett.* **103**, 242106 (2013).
29. B. Seger *et al.*, *J. Am. Chem. Soc.* **135**, 1057–1064 (2013).
30. B. Seger *et al.*, *RSC Adv.* **3**, 25902–25907 (2013).

ACKNOWLEDGMENTS

This work was supported by the Division of Chemical Sciences, Geosciences and Biosciences, Office of Basic Energy Sciences of the U.S. Department of Energy, through the Solar Photochemistry Program under contract no. DE-AC36-08GO28308 to the National Renewable Energy Laboratory. J.L.Y. acknowledges NSF Graduate Research Fellowship Grant no. DGE 1144083. The U.S. government retains—and the publisher, by accepting the article for publication, acknowledges that the U.S. government retains—a nonexclusive, paid-up, irrevocable, worldwide license to publish or reproduce the published form of this work, or allow others to do so, for U.S. government purposes.

SUPPLEMENTARY MATERIALS

www.sciencemag.org/content/350/6264/1061/suppl/DC1
Materials and Methods
Figs. S1 to S9
Tables S1 to S4
References (*31*, *32*)

31 August 2015; accepted 19 October 2015
10.1126/science.aad3459

NANOMATERIALS

Near-unity photoluminescence quantum yield in MoS_2

Matin Amani,[1,2]* Der-Hsien Lien,[1,2,3,4]* Daisuke Kiriya,[1,2]* Jun Xiao,[5,2] Angelica Azcatl,[6] Jiyoung Noh,[6] Surabhi R. Madhvapathy,[1,2] Rafik Addou,[6] Santosh KC,[6] Madan Dubey,[7] Kyeongjae Cho,[6] Robert M. Wallace,[6] Si-Chen Lee,[4] Jr-Hau He,[3] Joel W. Ager III,[2] Xiang Zhang,[5,2,8] Eli Yablonovitch,[1,2] Ali Javey[1,2]†

Two-dimensional (2D) transition metal dichalcogenides have emerged as a promising material system for optoelectronic applications, but their primary figure of merit, the room-temperature photoluminescence quantum yield (QY), is extremely low. The prototypical 2D material molybdenum disulfide (MoS_2) is reported to have a maximum QY of 0.6%, which indicates a considerable defect density. Here we report on an air-stable, solution-based chemical treatment by an organic superacid, which uniformly enhances the photoluminescence and minority carrier lifetime of MoS_2 monolayers by more than two orders of magnitude. The treatment eliminates defect-mediated nonradiative recombination, thus resulting in a final QY of more than 95%, with a longest-observed lifetime of 10.8 0.6 nanoseconds. Our ability to obtain optoelectronic monolayers with near-perfect properties opens the door for the development of highly efficient light-emitting diodes, lasers, and solar cells based on 2D materials.

Monolayer transition metal dichalcogenides (TMDCs) have properties that make them highly suitable for optoelectronics (*1*, *2*), including the ability to form van der Waals heterostructures without the need for lattice matching (*3*, *4*), circular dichroism arising from the direct band gap occurring at the K and K′ points of the Brillouin zone (*5*), and widely tunable band structure through the application of external forces such as electric field and strain (*6*). Unlike III-V semiconductors, the optical properties of TMDCs are dominated by excitons with strong binding energies (on the order of 300 meV) (*7*–*9*) and large radii (~1.6 nm) (*10*). However, TMDCs have exhibited poor luminescence quantum yield (QY)—that is, the number of photons the material radiates is much lower than the number of generated electron-hole pairs. QY values ranging from 0.01 to 6% have been reported, indicating a high density of defect states and mediocre electronic quality (*11*–*13*). The origin of the low quantum yield observed in these materials is attributed to defect-mediated nonradiative recombination and biexcitonic recombination at higher excitation powers (*11*, *13*).

Two-dimensional (2D) monolayers are amenable to surface passivation by chemical treatments. We studied a wide range of chemical treatments and describe here an air-stable, solution-based process using an organic superacid that removes the contribution of defect-mediated nonradiative recombination acting on electronically active defect sites by uniformly passivating them, repairing them, or both. With the use of this process, the photoluminescence (PL) in MoS_2 monolayers

---

[1]Electrical Engineering and Computer Sciences, University of California, Berkeley, Berkeley, CA 94720, USA. [2]Materials Sciences Division, Lawrence Berkeley National Laboratory, Berkeley, CA 94720, USA. [3]Computer, Electrical and Mathematical Sciences and Engineering Division, King Abdullah University of Science and Technology (KAUST), Thuwal 23955-6900, Saudi Arabia. [4]Department of Electrical Engineering, Institute of Electronics Engineering, National Taiwan University, Taipei 10617, Taiwan, Republic of China. [5]National Science Foundation Nanoscale Science and Engineering Center, University of California, Berkeley, Berkeley, CA 94720, USA. [6]Department of Materials Science and Engineering, University of Texas, Dallas, Richardson, TX 75080, USA. [7]Sensors and Electron Devices Directorate, U.S. Army Research Laboratory, Adelphi, MD 20723, USA. [8]Department of Physics, King Abdulaziz University, Jeddah 21589, Saudi Arabia.
*These authors contributed equally to this work. **†Corresponding author. E-mail: ajavey@eecs.berkeley.edu**

Fig. 1. Enhancement of PL by chemical treatment. (**A**) PL spectrum for both the as-exfoliated and TFSI-treated MoS_2 monolayers measured at an incident power of 1×10^{-2} W cm^{-2}. The inset shows normalized spectra. (**B** and **C**) PL images of a MoS_2 monolayer before (B) and after treatment (C). Insets show optical micrographs.

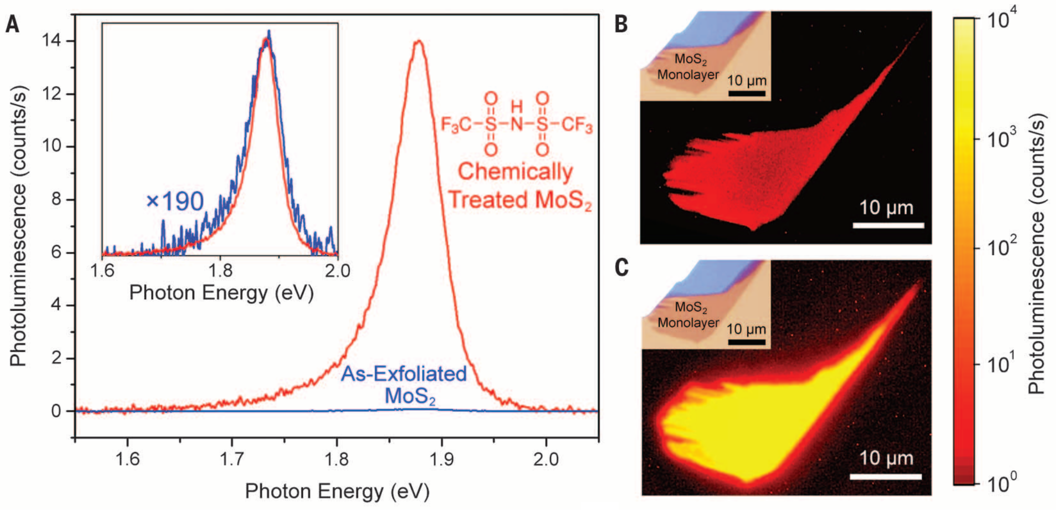

increased by more than two orders of magnitude, resulting in a QY > 95% and a characteristic lifetime of 10.8 ± 0.6 ns at low excitation densities.

In this study, we treated MoS_2 monolayers with a nonoxidizing organic superacid: bis(trifluoromethane) sulfonimide (TFSI). Superacids are strong protonating agents and have a Hammett acidity function (H_0) that is lower than that of pure sulfuric acid. [Details of the sample preparation and treatment procedure are discussed in the supplementary materials and methods (*14*).] The PL spectra of a MoS_2 monolayer measured before and after TFSI treatment (Fig. 1A) show a 190-fold increase in the PL peak intensity, with no change in the overall spectral shape. The magnitude of the enhancement depended strongly on the quality of the original as-exfoliated monolayer (*14*). (The term "as-exfoliated" indicates that the MoS_2 flakes were not processed after exfoliation.) PL images of a monolayer (Fig. 1, B and C, and fig. S4) (*14*), taken before and after treatment at the same illumination conditions, show that the enhancement from the superacid treatment is spatially uniform.

Calibrated steady-state PL measurements (*14*) showed that the spectral shape of the emission remained unchanged over a pump intensity dynamic range spanning six orders of magnitude (10^{-4} to 10^2 W cm^{-2}) (fig. S2) (*14*). From the pump-power dependence of the calibrated luminescence intensity (Fig. 2A), we extracted the QY (Fig. 2B). As-exfoliated samples exhibited low QY, with a peak efficiency of 1% measured at 10^{-2} W cm^{-2}. The absolute efficiency (*12*, *13*) and observed power law (*13*) are consistent with previous reports for exfoliated MoS_2. After TFSI treatment, the QY reached a plateau at a low pump intensity (<10^{-2} W cm^{-2}), with a maximum value greater than 95%. The near-unity QY suggests that, within this range of incident power, there was negligible nonradiative recombination occurring in the sample. Although pure radiative recombination is commonly observed for fluorescent molecules that inherently have no dangling bonds, only a few semiconductors, such as GaAs double heterostructures (*15*) and surface-passivated quantum dots (*16*), show this behavior at room temperature.

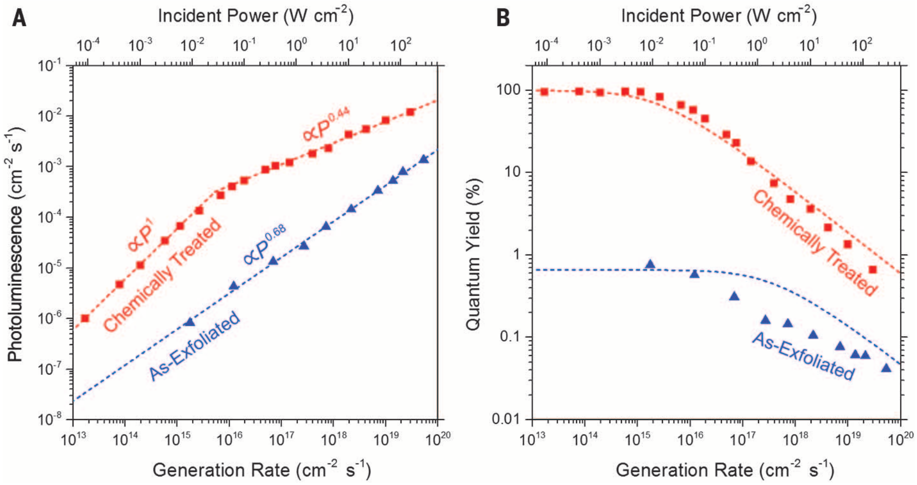

Fig. 2. Steady-state luminescence. (**A**) Pump-power dependence of the integrated PL for as-exfoliated and treated MoS_2. Dashed lines show power law fits for the three dominant recombination regimes. (**B**) Pump-power dependence of the QY for as-exfoliated and treated MoS_2. Dashed lines show the recombination model.

At high pump power, we observed a sharp drop-off in the QY, possibly caused by nonradiative biexcitonic recombination. We consider several models to explain the carrier density–dependent recombination mechanisms in MoS_2 before and after TFSI treatment. Here, n and p are the 2D electron and hole concentrations, respectively. At high-level injection, the dopant concentration is much less than the number of optically generated carriers, allowing $n = p$. The traditional interpretation without excitons (*17*) invokes a total recombination, R, as $R = An + Bn^2 + Cn^3$, where A is the Shockley-Read-Hall (SRH) recombination rate, B is the radiative recombination rate, and C is the Auger recombination rate. The QY is given as the radiative recombination rate over the total recombination. Auger processes dominate at high carrier concentrations, whereas SRH recombination dominates at low carrier concentrations. In the SRH regime (i.e., low pump power), QY increases with pump intensity. This behavior, however, was not observed in previous MoS_2 studies (*12*, *13*) or in this work.

The standard model poorly describes our QY data (fig. S10) (*14*), which are strongly influenced by bound excitons (*9*). As a result, the radiative rate is proportional to the total exciton population, $\langle N \rangle$ (*18*). At high exciton densities, nonradiative biexcitonic recombination can dominate, leading to a recombination rate proportional to $\langle N \rangle^2$ (*18*). Previous reports also suggest that the luminescence in as-exfoliated samples is limited by nonradiative defect-mediated processes (*19*, *20*), resulting in low QY. Although the precise nature of the defect-mediated nonradiative recombination is unclear, a simple analytical model can be developed to describe our experimental results. The total excitation rate, R, in MoS_2 is balanced by recombination

$$R = B_{nr}n^2 + B_r n^2 \tag{1}$$

where B_{nr} is the nonradiative defect-mediated recombination rate and B_r is the formation rate of excitons. The generated excitons can then either

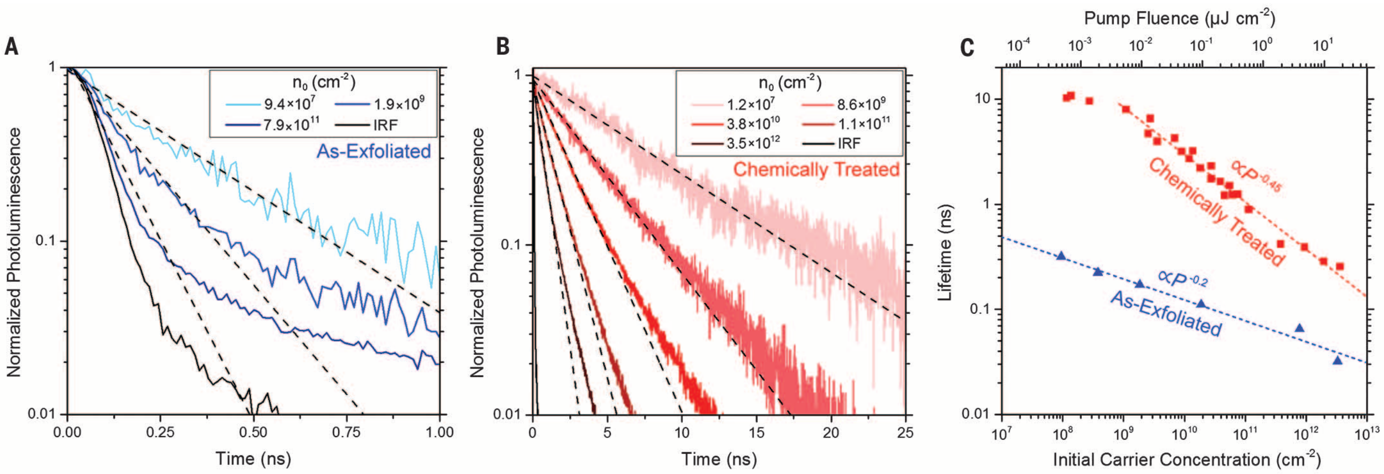

Fig. 3. Time-resolved luminescence. (**A**) Radiative decay of an as-exfoliated MoS_2 sample at various initial carrier concentrations (n_0), as well as the instrument response function (IRF). (**B**) Radiative decay of a treated MoS_2 sample plotted for several initial carrier concentrations (n_0), as well as the IRF. Dashed lines in (A) and (B) indicate single exponential fits. (**C**) Effective PL lifetime as a function of pump fluence. Dashed lines show a power law fit for the dominant recombination regimes.

undergo radiative recombination or nonradiatively recombine with a second exciton according to $B_r n^2 = \tau_r^{-1}\langle N\rangle + C_{bx}\langle N\rangle^2$ (*19*), where τ_r is the radiative lifetime and C_{bx} is the biexcitonic recombination rate. The QY is then given as

$$QY = \frac{\tau_r^{-1}\langle N\rangle}{\tau_r^{-1}\langle N\rangle + B_{nr}n^2 + C_{bx}\langle N\rangle^2} \qquad (2)$$

For the case of the TFSI-treated sample, B_{nr} is negligible because the QY at low pump powers is >95%, allowing us to extract a biexcitonic recombination coefficient C_{bx} = 2.8 $cm^2\ s^{-1}$. For the as-exfoliated sample, the defect-mediated nonradiative recombination can be fit to B_{nr} = 1.5 × 10^6 $cm^2\ s^{-1}$, using the same C_{bx} value. The fitting results are plotted as the dashed curves in Fig. 2B.

To investigate the carrier recombination dynamics, we performed time-resolved measurements on both as-exfoliated and chemically treated samples. The luminescence decay was nonexponential, but not in the standard form known for bimolecular (Bn^2) recombination (*17*). As-exfoliated monolayers of MoS_2 had extremely short lifetimes on the order of 100 ps (Fig. 3A and fig. S6) (*14*), consistent with previous reports (*21*). After treatment, we saw a substantial increase in the lifetime, which is shown at several pump fluences in Fig. 3A. Fitting was performed with a single exponential decay that described only the initial characteristic lifetime for a given pump intensity. After the pump pulse, the exciton population decayed, which resulted in nonexponential decay through reduced nonradiative biexcitonic recombination. At the lowest measurable pump fluences, we observed a luminescence lifetime of 10.8 ± 0.6 ns in the treated sample, compared with ~0.3 ns in the untreated case at a pump fluence of 5 × 10^{-4} μJ cm^{-2} (Fig. 3C). The contrast between panels A and B of Fig. 3 is consistent with the QY trend.

Urbach tails, which depict the sharpness of the band edges (*22*), were derived from the steady-state PL spectra via the van Roosbroeck–Shockley equation and are plotted in fig. S8. After treatment with TFSI, a noticeable decrease in the Urbach energy (E_0) from 17.4 to 13.3 meV was observed, indicating a reduction in the overall disorder from potential fluctuations and improved band-edge sharpness (*22*). A spatial map showing Urbach energy (fig. S8) (*14*) further indicates that the treatment was highly uniform. To evaluate stability, the QY in air for chemically treated MoS_2 was measured daily at a constant pump power over the course of 1 week, during which the sample was stored without any passivation in ambient lab conditions (20° to 22°C, 40 to 60% relative humidity), as shown in fig. S9 (*14*). The QY remained above 80% during this period, indicating that the treatment resulted in samples that were relatively stable.

We then turned our attention to the effect of TFSI treatment on other properties of MoS_2. The monolayer surface was imaged by atomic force microscopy (AFM) before and after treatment (Fig. 4A). No visible change to the surface morphology was observed. We also investigated the effect of the treatment on the electrical properties of a back-gated MoS_2 transistor. The transfer characteristics of this majority carrier device before and after treatment showed a shift in the threshold voltage toward zero, indicating that the native n-type doping in the MoS_2 was removed while the same drive current was maintained (Fig. 4B). An improvement in the subthreshold slope indicated that the treatment reduces interface trap states. The Raman spectra of an as-exfoliated and treated monolayer (Fig. 4C) showed that there was no change in the relative intensity or peak position. Thus, the structure of MoS_2 was not altered during treatment, and the lattice was not subjected to any induced strain (*23*). Because absolute absorption was used in the calibration of QY, we performed careful absorption measurements using two different methods (*14*), both before and after treatment (Fig. 4D). At the pump wavelength (514.5 nm), no measurable change of the absolute absorption from the treatment was observed. The strong resonances at 1.88 and 2.04 eV (corresponding to the A and B excitons, respectively) are consistent with previous reports (*12*). We then performed surface-sensitive x-ray photoelectron spectroscopy (XPS) on bulk MoS_2 from the same crystal used for micromechanical exfoliation. The Mo 3d and S 2p core levels (Fig. 4E) showed no observable change in oxidation state and bonding after treatment (*24*). Thus, an array of different techniques for materials characterization shows that the structure of the MoS_2 remains intact after TFSI treatment, with only the minority carrier properties (i.e., QY and lifetime) enhanced.

The effect of treatment by a wide variety of molecules is shown in table S1 and discussed in the supplementary text. Various polar, nonpolar, and fluorinated molecules, including strong acids and the solvents used for TFSI treatment (dichlorobenzene and dichloroethane), were explored. Treatment with the phenylated derivative of superacid TFSI was also performed (fig. S11) (*14*). These treatments all led to no or minimal (less than one order of magnitude) enhancement in PL QY.

The exact mechanism by which the TFSI passivates surface defects is not fully understood. Exfoliated MoS_2 surfaces contain regions with a large number of defect sites in the form of sulfur vacancies, adatoms on the surface, and numerous impurities (*25*–*27*). In fig. S12A (*14*), the calculated midgap energy is shown for several defect types, including a sulfur vacancy, adsorbed –OH, and adsorbed water. Deep-level traps—which contribute to defect-mediated nonradiative recombination, resulting in a low QY (*27*)—are observed for all of these cases. The strong protonating nature of the superacid can remove absorbed water, hydroxyl groups, oxygen, and other contaminants on the surface. Although these reactions will not remove the contribution of defects to nonradiative recombination, they will open the active defect sites to passivation by a second mechanism. One possibility is the protonation of the three dangling bonds at each sulfur vacancy site. However, density

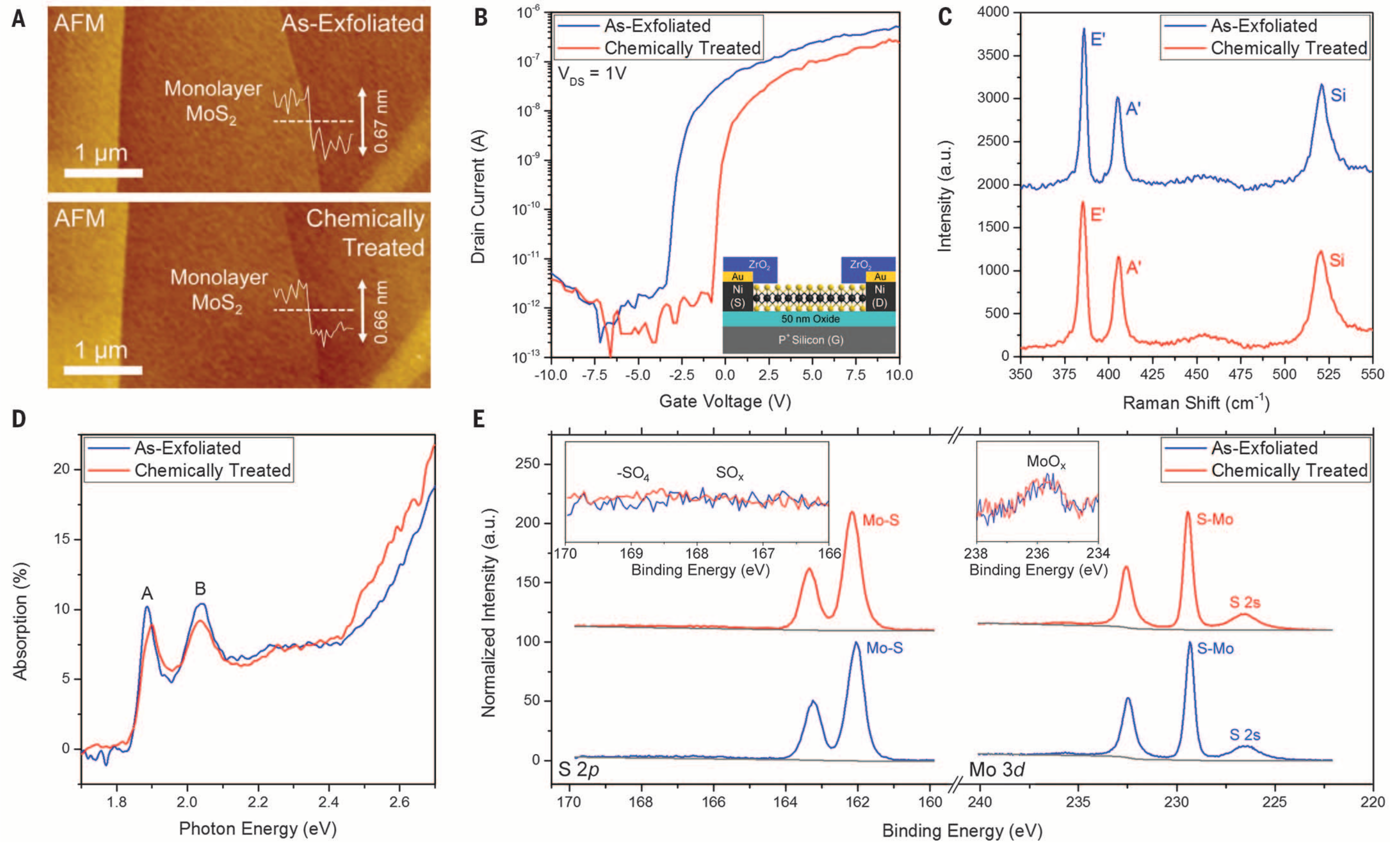

Fig. 4. Material and device characterization. (**A**) AFM images taken before and after TFSI treatment. (**B**) Transfer characteristics of a monolayer MoS_2 transistor, both before and after treatment. V_{DS}, drain-source voltage; S, source; D, drain; G, gate. (**C**) Raman spectrum of as-exfoliated and TFSI-treated MoS_2 samples. a.u., arbitrary units; E′, MoS_2 in-plane mode; A′, MoS_2 out-of-plane mode; Si, silicon Raman peak. (**D**) Absorption spectrum of the as-exfoliated and treated MoS_2 samples. A and B indicate the exciton resonances. (**E**) XPS spectrum of the S 2p and Mo 3d core levels before and after treatment. The insets show that there is no appearance of SO_x or change in the MoO_x peak intensity after treatment.

functional theory calculations (fig. S12C) (*14*) show that this reaction is energetically unfavorable. A second possibility is that the surface is restructured to reduce the sulfur vacancies through rearrangement of sulfur adatoms on the surface, which can be facilitated by hydrogenation via TFSI (*14*). The presence of sulfur adatom clusters has previously been confirmed by scanning tunneling microscopy and energy-dispersive x-ray spectroscopy (*27*–*30*). Careful examination of the XPS data over multiple spots before and after TFSI treatment (fig. S13) (*14*) reveals that the ratio of bonded sulfur to molybdenum (S/Mo) increased from 1.84 ± 0.04 in the as-exfoliated case to 1.95 ± 0.05 after treatment (table S2) (*14*).

We have demonstrated an air-stable process by which the PL of monolayer MoS_2 can be increased by more than two orders of magnitude, resulting in near-unity luminescence yield. This result sheds light on the importance of defects in limiting the performance of 2D systems and presents a practical route to eliminate their effect on optoelectronic properties. The existence of monolayers with near-ideal optoelectronic properties should enable the development of new high-performance light-emitting diodes, lasers, and solar cells. These devices can fulfill the revolutionary potential of the 2D semiconductors (*1*), which require interfacial passivation, as in all classic semiconductors.

REFERENCES AND NOTES

1. F. Xia, H. Wang, D. Xiao, M. Dubey, A. Ramasubramaniam, *Nat. Photonics* **8**, 899–907 (2014).
2. S. Wu *et al.*, *Nature* **520**, 69–72 (2015).
3. H. Fang *et al.*, *Proc. Natl. Acad. Sci. U.S.A.* **111**, 6198–6202 (2014).
4. L. Britnell *et al.*, *Science* **340**, 1311–1314 (2013).
5. K. F. Mak, K. He, J. Shan, T. F. Heinz, *Nat. Nanotechnol.* **7**, 494–498 (2012).
6. S. B. Desai *et al.*, *Nano Lett.* **14**, 4592–4597 (2014).
7. S. Tongay *et al.*, *Sci. Rep.* **3**, 2657 (2013).
8. A. Chernikov *et al.*, *Phys. Rev. Lett.* **113**, 076802 (2014).
9. H. M. Hill *et al.*, *Nano Lett.* **15**, 2992–2997 (2015).
10. T. C. Berkelbach, M. S. Hybertsen, D. R. Reichman, *Phys. Rev. B* **88**, 045318 (2013).
11. L. Yuan, L. Huang, *Nanoscale* **7**, 7402–7408 (2015).
12. K. F. Mak, C. Lee, J. Hone, J. Shan, T. F. Heinz, *Phys. Rev. Lett.* **105**, 136805 (2010).
13. H. Wang, C. Zhang, F. Rana, *Nano Lett.* **15**, 339–345 (2015).
14. Materials and methods are available as supplementary materials on *Science* Online.
15. I. Schnitzer, E. Yablonovitch, C. Caneau, T. J. Gmitter, *Appl. Phys. Lett.* **62**, 131–133 (1993).
16. Y. S. Park *et al.*, *Phys. Rev. Lett.* **106**, 187401 (2011).
17. P. T. Landsberg, *Phys. Status Solidi* **41**, 457–489 (1970).
18. F. Wang, Y. Wu, M. S. Hybertsen, T. F. Heinz, *Phys. Rev. B* **73**, 245424 (2006).
19. H. Wang *et al.*, *Phys. Rev. B* **91**, 165411 (2015).
20. C. Mai *et al.*, *Nano Lett.* **14**, 202–206 (2014).
21. T. Korn, S. Heydrich, M. Hirmer, J. Schmutzler, C. Schuller, *Appl. Phys. Lett.* **99**, 102109 (2011).
22. A. Iribarren, R. Castro-Rodriguez, V. Sosa, J. L. Pena, *Phys. Rev. B* **58**, 1907–1911 (1998).
23. Z. Liu *et al.*, *Nat. Commun.* **5**, 5246 (2014).
24. A. Azcatl *et al.*, *Appl. Phys. Lett.* **104**, 111601 (2014).
25. C. P. Lu, G. Li, J. Mao, L. M. Wang, E. Y. Andrei, *Nano Lett.* **14**, 4628–4633 (2014).
26. S. McDonnell, R. Addou, C. Buie, R. M. Wallace, C. L. Hinkle, *ACS Nano* **8**, 2880–2888 (2014).
27. R. Addou *et al.*, *ACS Nano* **9**, 9124–9133 (2015).
28. R. Addou, L. Colombo, R. M. Wallace, *Appl. Mat. Interfaces.* **7**, 11921–11929 (2015).
29. J. Y. Noh, H. Kim, Y. S. Kim, *Phys. Rev. B* **89**, 205417 (2014).
30. A. P. Nayak *et al.*, *Nat. Commun.* **5**, 3731 (2014).

ACKNOWLEDGMENTS

We thank F. R. Fischer for in-depth discussions on surface chemistry and A. B. Sachid for analysis of the electrical measurements. M.A., J.X., J.W.A., X.Z., and A.J. were funded by the Director, Office of Science, Office of Basic Energy Sciences, Materials Sciences and Engineering Division of the U.S. Department of Energy, under contract no. DE-AC02-05Ch11231. A.A., J.N., R.A., S.KC, R.M.W., and K.C. were funded by the Center for Low Energy System Technology (LEAST), one of six centers supported by the STARnet phase of the Focus Research Program (FCRP), a Semiconductor Research Corporation program sponsored by Microelectronics Advanced Research Corporation and Defense Advanced Research Projects Agency. D.K. acknowledges support from Samsung, E.Y. acknowledges support from the NSF Center for Energy Efficient Electronics Science (E^3S), J.-H.H. acknowledges support from the baseline fund of KAUST, and M.D. acknowledges support from the U.S. Army Research Lab Director's Strategic Initiative program on interfaces in stacked 2D atomic layers and materials.

SUPPLEMENTARY MATERIALS

www.sciencemag.org/content/350/6264/1065/suppl/DC1
Materials and Methods
Supplementary Text
Figs. S1 to S13
Tables S1 and S2
References (*31*–*48*)

12 August 2015; accepted 13 October 2015
10.1126/science.aad2114

www.sciencemag.org/content/350/6264/1065/suppl/DC1

Supplementary Materials for

Near-unity photoluminescence quantum yield in MoS_2

Matin Amani, Der-Hsien Lien, Daisuke Kiriya, Jun Xiao, Angelica Azcatl, Jiyoung Noh, Surabhi R. Madhvapathy, Rafik Addou, Santosh KC, Madan Dubey, Kyeongjae Cho, Robert M. Wallace, Si-Chen Lee, Jr-Hau He, Joel W. Ager III, Xiang Zhang, Eli Yablonovitch, Ali Javey*

*Corresponding author. E-mail: ajavey@eecs.berkeley.edu

Published 27 November 2015, *Science* **350**, 1065 (2015)
DOI: 10.1126/science.aad2114

This PDF file includes:

Materials and Methods
Supplementary Text
Figs. S1 to S13
Tables S1 and S2
Full Reference List

Materials and Methods

1. Sample Preparation and Solution Treatment Procedure

MoS_2 (SPI Supplies) was mechanically exfoliated on either quartz for quantum yield (QY), lifetime, and absorption measurements or on SiO_2/Si substrates for imaging, electrical, and Raman characterization. Monolayers were identified by optical contrast and atomic force microscopy (AFM). The treatment procedure with bis(trifluoromethane)sulfonimide (TFSI) is as follows: 20 mg of TFSI, (Sigma-Aldrich) was dissolved in 10 ml of 1,2-dichloroethane (DCE) (Sigma-Aldrich) to make a 2 mg/ml solution. The solution is further diluted with 1,2-dichlorobenzene (DCB) (Sigma-Aldrich) or DCE to make a 0.2 mg/ml TFSI solution. The exfoliated sample was then immersed in the 0.2 mg/ml solution in a tightly closed vial for 10 min on a hotplate (100°C). The sample was removed and blow dried with nitrogen without rinsing and subsequently annealed at 100°C for 5 min. Depending on the initial optical quality of the sample, the treatment sometimes needed to be repeated to obtain > 95% QY. As a control experiment we studied N-phenyl-bis(trifluoromethane)sulfonimide (Ph-TFSI) which was prepared using the following procedure: 25 mg of Ph-TFSI (Sigma-Aldrich) was dissolved in 10 ml of DCE (Sigma-Aldrich) to make a 2.5 mg/ml solution. The solution is further diluted with DCB (Sigma-Aldrich) to a 0.25 mg/ml solution. The exfoliated sample was immersed in the 0.25 mg/ml solution in a tightly capped vial for 10 min on a hotplate (100 °C). The sample was removed and blow dried with nitrogen without rinsing and subsequently annealed at 100°C for 5 min. Prior to treatment, samples were annealed in forming gas (5% H_2, 95% N_2) at 300°C for 3 hours; while this does not significantly affect the QY after treatment it was found to significantly improve the long term stability of the sample. It is important to note that there is a large variation in the QY of as-exfoliated monolayer samples (with peak QY ranging from 0.1% to 1%). All data taken on as-exfoliated monolayers in this manuscript are representative of samples with a peak QY close to 1%.

2. Calibrated Luminescence Efficiency Measurements

The PL (photoluminescence) data presented here was obtained with a custom built micro-PL system using the 514.5 nm line of an Ar ion laser (Lexel 95) for excitation. The laser power was adjusted using various neutral density (ND) filters. An overview of the configuration used for measurement and the calibration of the instrument is shown in Fig. S1. The power of the excitation beam was measured during the duration of the measurement (130 times greater than the incident power on the sample) and was calibrated at high illumination intensity using a photodiode power meter (ThorLabs S120C). However, in order to accurately measure low (< 100 pW) excitation power, lock-in detection from the output of a calibrated photodiode was used (noise equivalent power of 1.7×10^{-13} W $\mathrm{Hz}^{-1/2}$). These values were carefully cross calibrated before all measurements at multiple laser powers to ensure the incident power was accurately measured. The laser beam was focused onto the sample using a 60× ultra-long working distance (ULWD) objective lens (NA = 0.7) which resulted in a measured spot size of 3.8 μm^2. PL was collected by the same microscope objective, passed through a 550 nm dielectric longpass filter to remove the excitation signal, dispersed by an f = 340 mm spectrometer with either a 150 g/mm or 600 g/mm grating, and detected by a Si CCD camera (Andor iDus BEX2-DD). The CCD background was obtaining by collecting a spectrum before each measurement at the same integration time without the laser on and was subsequently subtracted from the PL spectrum. We calculated the error in the integrated counts using:

$$\delta N = \frac{N}{\sqrt{N + n_{pix}\left(1 + \frac{n_{pix}}{n_b}\right)N_{RO}^2}}$$

where δN is signal to noise ratio, N is the total PL counts, n_{pix} is the number of pixels, n_b is the uncertainty from the background estimation, and N_{RO} is the readout noise (*31*).

Prior to measuring, the entrance slit of the spectrometer was opened until the maximum number of PL counts was obtained. All measurements were performed using linearly polarized excitation, negating any effects from intervalley scattering by maintaining equivalent population in two valleys (*32*).

The spectrometer wavelength was calibrated using the atomic emission peaks from Ar and Kr lamps (Newport). The systems' relative sensitivity versus wavelength (instrument function) was evaluated by measuring the response of a virtual Lambertian black body light source created under the objective via illumination from a temperature stabilized lamp (ThorLabs SLS201) imaged onto a diffuse reflector (> 1 cm thick spectralon) surface. The system efficiency was calibrated immediately after each measurement by removing the 550 nm long pass filter and measuring the response of the excitation laser focused on the diffuse reflector (> 1 cm thick spectralon). This is a reasonable simulation of the PL source, as the emission profile of 2D materials has recently been experimentally measured and is approximately Lambertian (*33*). The pump-power dependence is converted to external quantum efficiency (EQE) by dividing by the absorbed pump power (*P*), i.e.: $EQY = PL / P$.

Two independent approaches were used to verify the system calibration. First, to remove the possibility of errors due to the confocal nature of the spectral measurement, which is strongly dependent on the objective focus and the solid angle covered by the collection cone, we cross-calibrated using a calibrated silicon photodiode which was able to view a fraction of the luminescence but is independent of microscope optical path as depicted in Fig. S1; due to the relatively low sensitivity of the photodiode, these measurements were only performed at higher excitation power (> 10 W cm^{-2}). Calibrations were also performed using a sample with a known QY close to 100% (rhodamine 6G in methanol) (*34*) using a procedure which has previously been used to measure the QY of 2D materials (*12, 13*). These three methods were found to be in good agreement with each other (< 15% error). For measurements taken against the spectralon reference the percent of generated photons which are able to escape from the sample was calculated using $1/4n^2$, where n is the refractive index of the medium, this was used to determine the QY from the measured EQE (*35*).

The error in the QY measurements was calculated from the uncertainty in the laser power measurement, CCD signal, and the absorption coefficient. The overall error bounds for the measurement are given by:

$$\delta QY = QY\sqrt{\left(\frac{\delta P}{N}\right)^2 + \left(\frac{\delta N}{N}\right)^2 + \left(\frac{\delta \alpha}{N}\right)^2}$$

where, P and δP is the measured laser power and the corresponding uncertainty, N and δN is the measured CCD counts and corresponding uncertainty, and α and $\delta\alpha$ is the absorption coefficient at 514.5 nm and the corresponding uncertainty.

The normalized PL spectra used to generate the QY data shown in Fig. 2A and 2B are depicted in Fig S2. There is no observable change in the PL emission spectral shape as a function of pump power, indicating that we see no luminescence from biexcitonic recombination or through a secondary radiative mechanism.

3. Micro-Absorption and Reflection Measurements

Two sets of absorption/reflection measurements were performed for monolayer MoS_2 on quartz substrates both before and after treatment. First the absolute absorption at the PL excitation wavelength (514.5 nm) was measured using lock-in detection; a schematic of the setup is shown in Fig. S3A. The extracted absorption value of 7.53±0.23% is used for the QY calculations. Illumination from a supercontinuum laser source (Fianium WhiteLase SC-400) was used to obtain an absorption spectrum (total incident power << 1 W cm^{-2}). Either the reflected or transmitted light was guided to a spectrometer to analyze the full spectrum. A schematic of the setup is shown in Fig. S3B. In both cases the light was focused on the sample using a 50× objective, the reflected light was collected via the same objective and the transmitted light was collected by a 20× objective. The system was calibrated using quartz and silver as reference transmission and reflectance standards. The reported generation rates (steady-state measurements) and initial carrier densities (time-resolved measurements) are calculated from the number of incident photons per unit area and the absorption.

4. Other Optical Methods

All measurements were taken starting from the lowest laser power and were stopped at a maximum power (10 μW) approximately one order of magnitude lower than what was found to cause sample degradation. The TFSI treated samples in particular were found to be sensitive to high illumination powers. An important consideration for MoS_2 is that the thickness of the sample (0.7 nm) is significantly less than the emission wavelength, thus the refractive index of the surrounding medium will determine the optical mode density and influence the measured lifetime according to the Füchtbauer-Ladenburg equation:

$$\frac{1}{\tau_r} = 8\pi n^2 c \int \frac{\sigma_{em}(\lambda)}{\lambda^4} d\lambda$$

which is an extension of the Einstein A and B coefficients where τ_r is the radiative lifetime, n is the refractive index of the medium, c is the speed of light in vacuum, σ_{em} is the emission cross-section, and λ is the wavelength of spontaneous emission (*36*, *37*). Therefore, we utilized quartz substrates for all measurements where an absolute QY and/or radiative lifetime is reported. It is important to note that in the case of samples with low luminescence (< 10% QY) the measured lifetime will be dominated by the nonradiative lifetime (τ_{nr}) and therefore approximately equal to τ_{nr}, ergo this effect will not play a dominant role.

Raman spectra was measured with a triple spectrometer configured in subtractive mode with a 2400 g/mm grating in the final stage and using the 514.5 nm line of the Ar ion laser as the excitation source. PL imaging was performed using a florescence microscopy setup with a 470 nm LED excitation source (operating at 200 mA) and a CCD detector (Andor Luca). The background counts were subtracted from the PL images and cosmic rays were removed using a software filter; the images were then normalized by integration time. High resolution PL mapping was performed using a WITec Alpha 300RA equipped with a piezo electric scanning stage. The sample was excited using the 532 nm line of a frequency-doubled Nd:YAG laser as the excitation source and focused on the sample using a 100× objective.

For time-resolved photoluminescence performed on treated MoS_2, the sample was excited pulsed light at 5 MHz generated by a supercontinuum laser source (Fianium WhiteLase SC-400) (20-30 ps pulse width). A wavelength of 514 nm (2 nm measured bandwidth) was selected with a monochrometer and was subsequently sent through a bandpass filter to remove any stray leakage light. The excitation was linearly polarized and focused on the sample with a 60× ULWD objective. The signal was detected with a low dark count avalanche photodiode operating in single photon counting mode (IDQuantiqe) and analyzed using a time correlated single photon counting module (TCSPC) (Becker-Hickl GmbH). The instrument response was 110 ps and the data was fit by deconvolution from the instrument response to a single exponential decay; the reported errors are the uncertainty from fitting.

Due to the extremely short lifetime of as-exfoliated MoS_2 monolayers, time-resolved measurements were also performed via a synchroscan streak camera (Hamamatsu) with an overall time resolution of 2 picoseconds as shown in Fig. S6. The sample was excited by 560 nm light generated by an optical parametric oscillator (Spectra Physics, Inspire HF 100) pumped by a mode-locked Ti:sapphire oscillator. The laser pulse width was 200 femtoseconds, and the repetition rate was 80 MHz. The linearly polarized excitation light was guided to an inverted microscope and focused on the sample by a 50× objective. The emission signal was detected in the back scattering configuration using emission filters to block the excitation laser prior to collection.

The band edge tail *D(υ)* (also known as the Urbach tail) can be related to the photon emission rate per unit energy at steady-state conditions by the van Roosbroeck-Schockley equation:

$$D(\nu) \propto \frac{I(\nu)\left(e^{h\nu/kT}-1\right)}{n_r^2\nu^2}$$

where, h is the Plank constant, k is the Boltzmann constant, T is temperature, and n_r is the real part of the refractive index (*22*). From this we can extract the Urbach parameter, E_0 (characteristic width of the absorption edge) using:

$$D(h\nu) = D_0 e^{\left(h\nu - E_g\right)/E_0}$$

where E_g is the bandgap. The band edge tail for a sample before and after treatment is plotted in Fig. S8, and shows an improvement in the Urbach parameter from 17.4 meV to 13.3 meV, indicating reduced defects at the band edge and reduced lattice disorder. A spatial map of the Urbach parameter of a treated sample (insert of Fig. S8) shows that it is highly uniform.

5. Device Fabrication and Measurement

Back gated single layer thick MoS_2 transistors were fabricated on Si/SiO_2 substrates with a 50 nm thick oxide using standard e-beam lithography techniques. After patterning the flakes via dry etching by XeF_2, Ni/Au (10 nm/40 nm) contacts were deposited by e-beam evaporation. TFSI was found to attack Ni, even with an Au capping layer; as a result the treatment severely degrades the performance of the contacts and has a large negative impact on device performance. In order to mitigate this a 20 nm thick ZrO_2 barrier was grown by ALD directly over the contact regions to protect them during treatment, while leaving the MoS_2 channel exposed to the TFSI. Devices were measured in air using an Agilent 4155C parameter analyzer.

6. X-Ray Photoelectron Spectroscopy

X-ray photoelectron spectroscopy (XPS) was carried out using a monochromated Al Kα source (hν = 1486.7 eV) and an Omicron EA125 hemispherical 7-channel analyzer. The XPS scans were acquired at a take-off angle of 45° with respect to the sample normal and pass energy of 15 eV. For XPS peak analysis and deconvolution, the software AAnalyzer was employed, where Voigt line shapes and an active Shirley background were used for peak fitting. The S/Mo ratios were determined from the integrated areas of the S *2p* and Mo *3d* peaks factored by their corresponding relative sensitivity factors. The error in the S/Mo ratios was obtained from the peak fitting residuals given by the AAnalyzer software.

Prior to superacid treatment, XPS scans were performed on crystals from the same bulk MoS_2 source (SPI Supplies) which was prepared by micromechanical exfoliation. Then, the MoS_2 sample was submerged in a superacid solution of 2 mg of TFSI in 10 ml of DCE for 10 minutes. The sample was removed and blow dried with nitrogen without rinsing and subsequently annealed at 100°C for 5 min. The TFSI treated MoS_2 sample was loaded into UHV within five minutes for XPS analysis. To minimize contamination, the TFSI treatment was performed in Teflon labware which was cleaned by piranha solution followed by a DI water rinse. Monolayer samples prepared using this clean treatment procedure were found to also show a QY of > 95%.

7. Calculation of Defect Band Structure and Defect Formation Energy

Theoretical calculations based on density functional theory (DFT) (*38*, *39*) were performed with plane wave basis sets and Projector Augmented Wave (PAW) pseudopotentials (*40*, *41*) as implemented in the Vienna *ab initio* simulation package (VASP) (*42*). A kinetic energy cutoff of 500 eV for the plane-wave basis set expansion is used. The exchange-correlation interactions are incorporated as a functional of Generalized Gradient Approximation (GGA) in the present work. A monolayer of 5x5 supercell of MoS_2 surface model constructed to investigate the MoS_2 surface. In the self-consistent field calculations, a Γ-centered 6x6x1 k-point mesh is employed for the supercell and a 12x12x1 k-point mesh is employed for density of states (DOSs) calculations. A monolayer of MoS_2 contains two atomic layers of sulfur and one atomic layer of molybdenum, which are periodically repeated. Each periodic layer is separated by ~16 Å of vacuum to avoid interaction between the two surfaces of the layer and their replica images. In this work, the atomic structures are relaxed until energy and Hellmann-Feynman force convergence criteria are less than 10^{-4} eV and 0.01 eV/Å, respectively, while the cell size was kept after the as-exfoliated surface was fully relaxed. The in-plane lattice constant (a) is calculated 3.16 Å in single-layer MoS_2. The formation energy of the defect is calculated by:

$$E_{form}^{defect} = E(defect) - E(MoS_2) - \sum_i N_i \mu_i$$

where E(defect) is the total energy of a single-layer MoS_2 containing a defect in the supercell, $E(MoS_2)$ is the total energy per a supercell of an as-exfoliated single-layer MoS_2 without a defect, N_i is the number of *i* element added (or removed) in the supercell, μ_i is the chemical potential of the element *i* (*43*). In S-deficiency condition, $\mu_S = (\mu_{MoS2} - \mu_{Mo})/2$, where μ_{MoS2} is the total energy of the as-exfoliated monolayer MoS_2 per a formula unit and μ_{Mo} is the total energy of a Mo bcc metal per an atom. We obtained the chemical potential of oxygen and hydrogen from gas phase O_2 and H_2, respectively.

Negative formation energy indicate that the surface is thermodynamically favorable to contain defects.

Supplementary Text

1. Recombination Model

In the recombination model typically used for III-V semiconductors, the total recombination is given by $R = An + Bnp + Cn^2 p$, where A is the Shockley-Reed-Hall recombination, B is the radiative recombination, C is Auger recombination, and n and p are the 2D electron and hole concentrations respectively (*44*). The QY is then expressed as the ratio of the radiative rate over total recombination, yielding:

$$QY = \frac{Bnp}{An + Bnp + Cn^2 p}$$

As a first pass, this model (using 2D carrier densities) was used to describe the recombination kinetics observed in MoS_2 and is plotted as dotted curves in Fig. S10 (Treated: A = 0 s^{-1}, B = 1×10^{12} $cm^2 s^{-1}$, C = 5×10^{10} $cm^4 s^{-1}$; As-exfoliated: A = 0 s^{-1}, B = 1.6×10^{10} $cm^2 s^{-1}$, C = 5×10^{10} $cm^4 s^{-1}$). While this model provides a good fit to the as-exfoliated data which indicates that there may be an Auger like (three-particle) dependence on carrier density, it fails to accurately capture the behavior of the treated sample. Since MoS_2 is excitonic system (*12*), the standard semiconductor model was modified to incorporate the formation of excitons from free carriers and a second generation-recombination balance equation was written for the exciton population. In its simplest form, neglecting any recombination mechanisms this is given by: $R = Bn^2$ and $Bn^2 = \tau_{rad}^{-1}\langle N\rangle$, where $\langle N\rangle$ is the exciton concentration. Several recombination mechanism were considered; however, we chose to implement only biexcitonic recombination (intrinsic material property) and defect-mediated nonradiative recombination of free carriers (extrinsic material property). The resulting balance equations have the form:

$$R = B_r n^2 + B_{nr} n^2$$

and

$$B_r n^2 = \tau_r^{-1}\langle N\rangle + C_{bx}\langle N\rangle^2$$

where, B_r is the formation rate of excitons, B_{nr} is defect mediated nonradiative recombination of two free carries and a deep level trap, τ_r is the exciton radiative lifetime, and C_{bx} is the biexcitonic recombination coefficient. The QY is then given as:

$$QY = \frac{\tau_r^{-1}\langle N\rangle}{\tau_r^{-1}\langle N\rangle + B_{nr}n^2 + C_{bx}\langle N\rangle^2}$$

The exciton formation is coupled to τ_r, however, in the experiments discussed here, the two parameters cannot be distinguished. Thus, B_r was arbitrarily set as 1×10^4 cm^2 s^{-1} and τ_r was set to the longest measured lifetime (10 nanoseconds). The fitting results are plotted in Fig. S10. A biexcitonic recombination coefficient of 2.8 cm^2 s^{-1} was used in both the as-exfoliated and treated sample, and the defect mediated nonradiative recombination coefficient was increased from 0 cm^2 s^{-1} in the case of treated MoS_2 to 1.5×10^6 cm^2 s^{-1} for as-exfoliated. The fitting is in reasonable agreement with the experimental data. Moreover it manages to effectively describe the data using previously reported recombination mechanisms.

2. Control Treatments

To better understand the role of surface chemical treatments on the QY of MoS_2, many treatments were performed in a variety of different molecules; the results are summarized in Table S1. Treatments in common hydroxide based species such as water and alcohol did not show PL enhancement. It is likely that the surface and defects in MoS_2 have already been exposed to air and moisture before treatments, and the defects on the surface are likely filled by adsorbed water or -OH groups. On the other hand, in cases of chlorine based treatments (DCE, DCB) a marginal PL enhancement was observed. This result indicates that there is a relatively strong interaction between chlorine-based molecules and the surface of MoS_2, which was reported previously for DCE (*45*). This motivated the selection of DCB/DCE (9/1 v/v%) as the solvent choice for treatment by TFSI, which was found to give the optimum treatment conditions, although other solvents were also effective.

To clarify the role of TFSI in passivating the surface of MoS_2, N-Phenyl-bis(trifluoromethanesulfonimide) (Ph-TFSI) was introduced as a control reagent. MoS_2

monolayers were treated with Ph-TFSI in a solution of DCB/DCE (9/1 v/v%) using the identical treatment procedure as TFSI (materials and methods). Fig. S11 shows the pump-power dependence on PL and QY for Ph-TFSI treated and as-exfoliated monolayers. The Ph-TFSI solution does not significantly alter the QY relative to the original as-exfoliated sample. Considering that the only difference between TFSI and Ph-TFSI is the replacement of hydrogen with a phenyl group, hydrogen is believed to play a critical role in the passivation of defect sites leading to the enhancement of QY.

A wide variety of possible defect sites have been observed in MoS_2, both through scanning tunneling microscopy (STM) or through transmission electron microscopy (TEM) (*28, 46*). The DoS for the most commonly observed defect, sulfur vacancies (V_s) as well as a vacancy site with an adsorbed –OH group are shown in Fig. S12A. Both of these scenarios induce midgap trap states which can induce defect-mediated recombination and quench the PL. To determine the possible mechanism of the treatment we examined several plausible scenarios. Firstly, due to the high stability of its ionic state, which arises from the delocalization of the anion charge on the nitrogen it is highly unlikely that the TFSI anion passivates the surface. Passivation of dangling bonds at the vacancy site by hydrogen was also considered, and DoS calculations show that the midgap states are removed when the three dangling bonds which occur at the sulfur vacancy site are passivated by hydrogen as shown in Fig. S12B. This scenario was also found to be improbable however, since it is highly energetically unfavorable (Fig. S12C); additionally, hydrogenation of Mo in MoS_2 has been found to be unlikely in previous reports (*47, 48*).

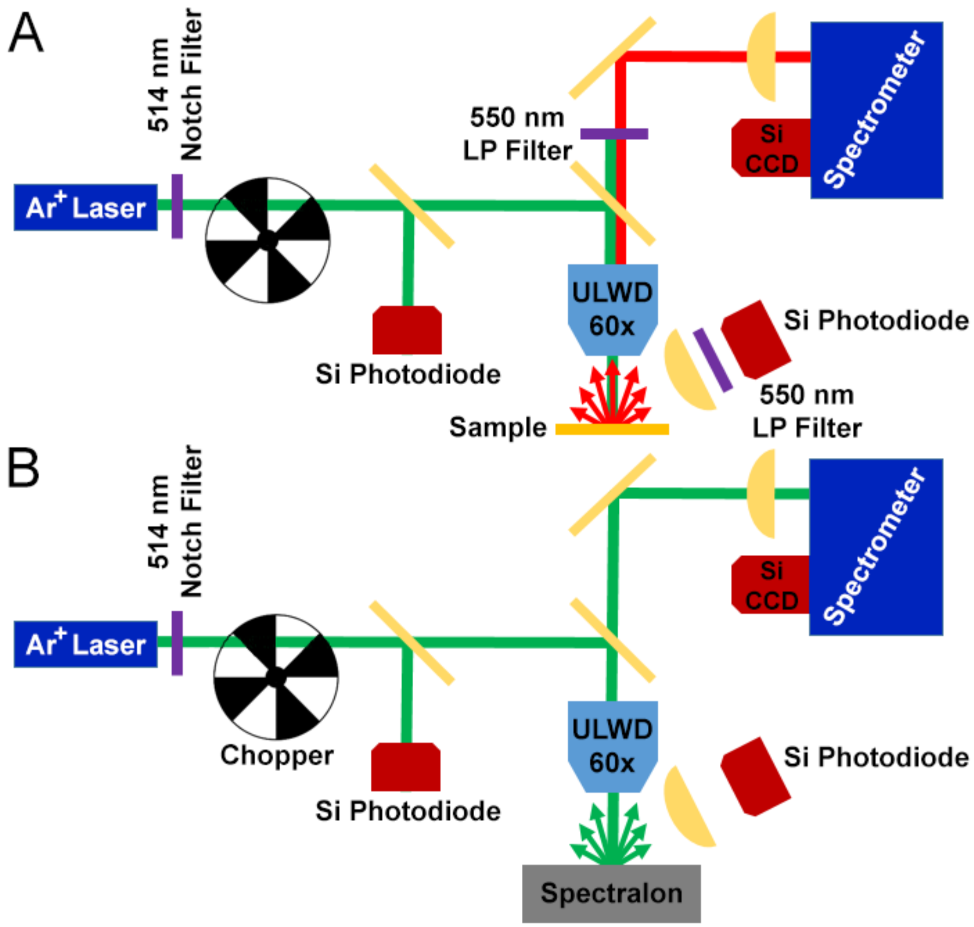

Fig. S1. Schematic of the optical setup used to measure external quantum efficiency. (**A**) Optical setup used to measure PL spectrum as well as calibration via a R6G film. (**B**) Optical setup used for calibrating the absolute collection efficiency via a near ideal diffuse reflector.

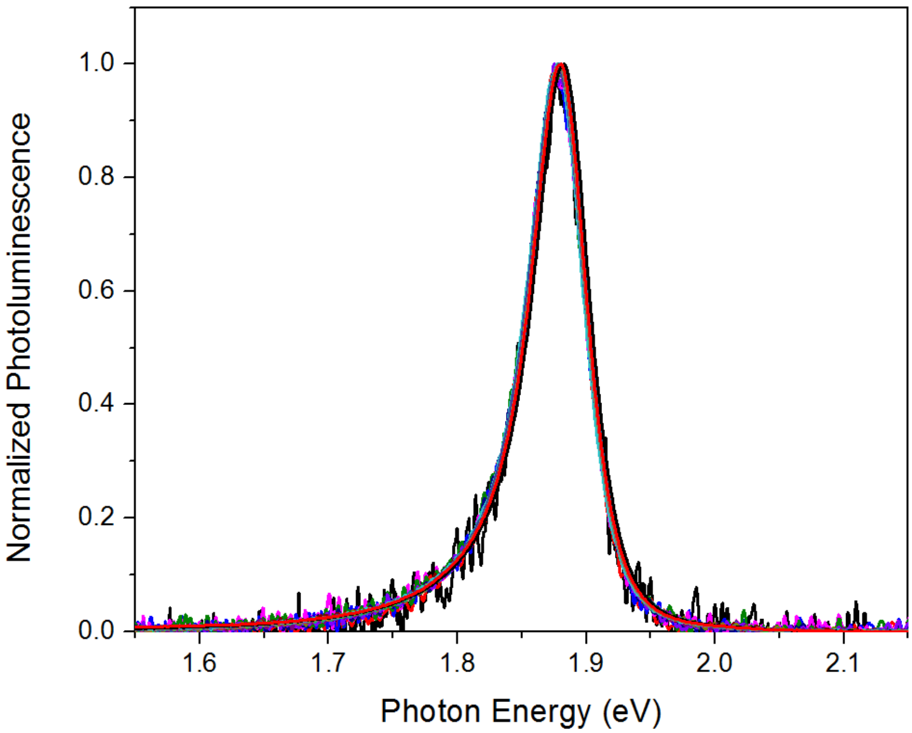

Fig. S2. Normalized PL spectrum at various pump-power. Normalized PL data used to calculate QY for TFSI treated samples shown in Fig. 2A and 2B (26 curves are overlaid). No apparent changes in the PL spectral shape are observed as the incident power is varied over the full range of incident powers (from 10^{-4} W cm^{-2} to 10^{2} W cm^{-2}).

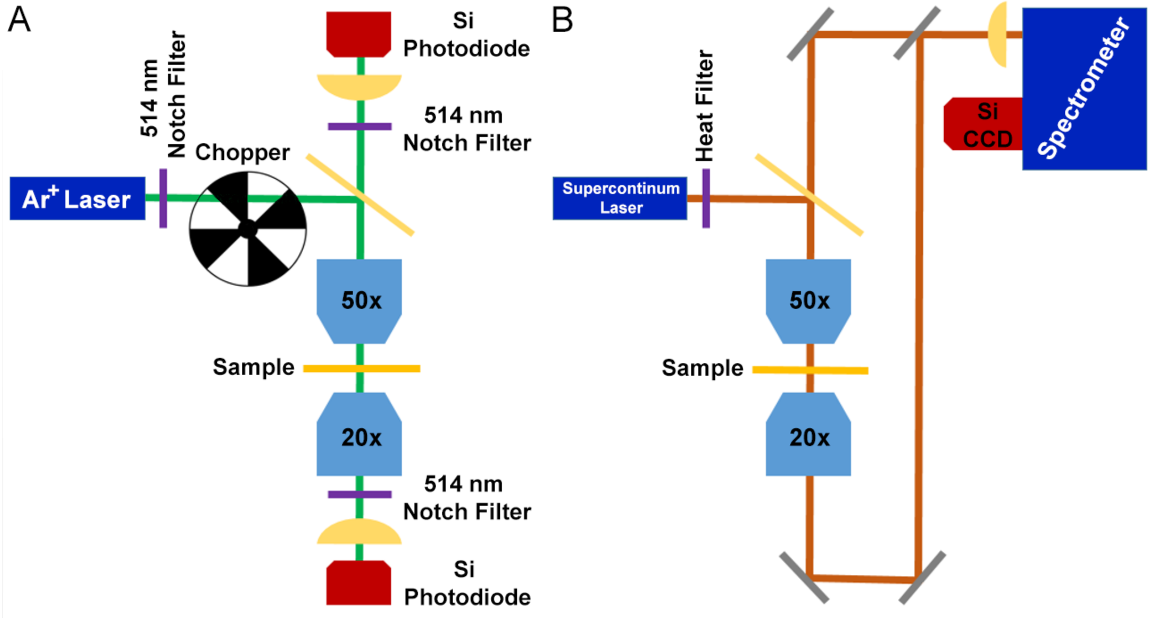

Fig. S3. Schematic of the optical setup used to measure absorption. (**A**) Optical setup used to measure the absorption at 514.5 nm. (**B**) System configuration used to measure the full absorption spectrum via separately measuring the transmitted and reflected light from a white laser source.

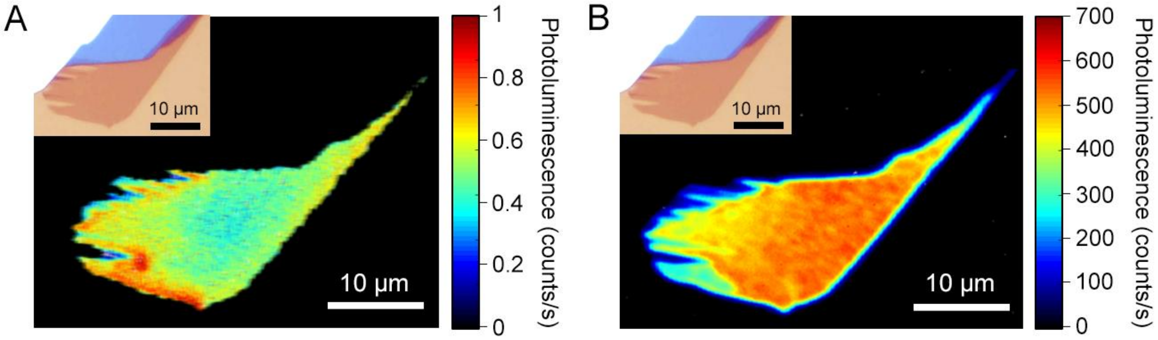

Fig. S4. Linear scale photoluminescence images. (**A**) Linear scale PL image for the as-exfoliated monolayer shown in Fig. 1B; scale bar is 10 μm. (**B**) Linear scale PL image for the treated monolayer shown in Fig. 1C; scale bar is 10 μm.

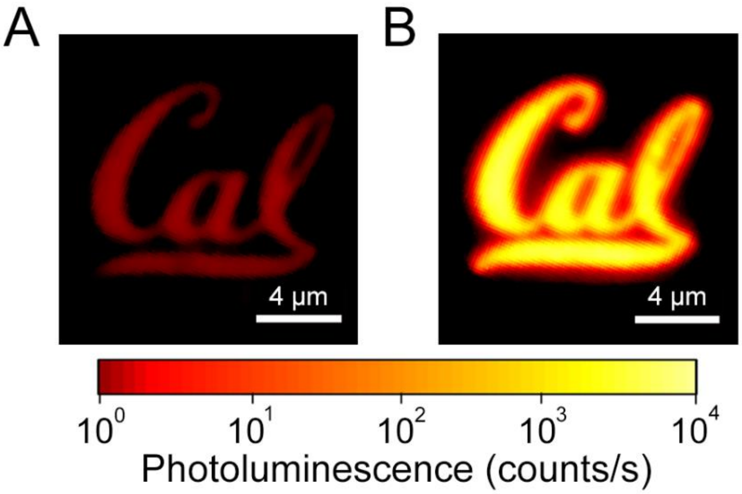

Fig. S5. Photoluminescence image of patterned monolayer. (**A**) PL image for a monolayer patterned by e-beam lithography into the shape of the Berkeley "Cal" logo. (**B**) PL image for the same patterned monolayer after treatment by TFSI.

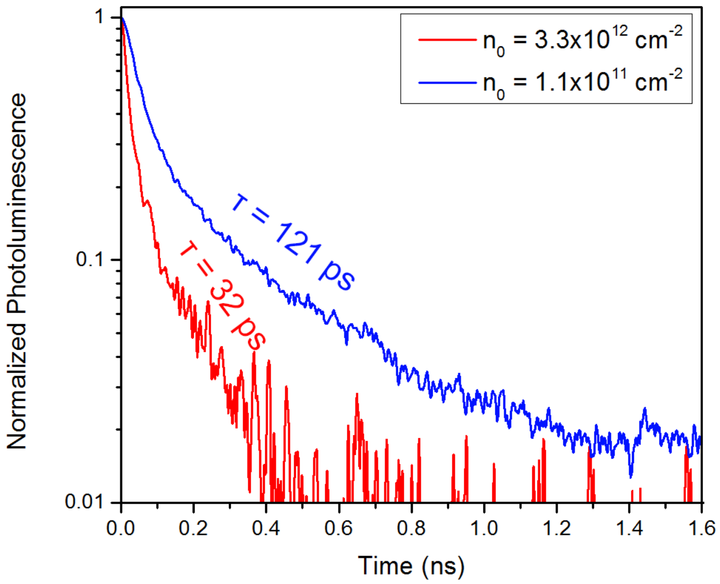

Fig. S6. As-exfoliated MoS_2 time-resolved luminescence. Photoluminescence decay spectrum for as-exfoliated MoS_2 measured at multiple excitation powers using a streak camera (2 ps timing resolution).

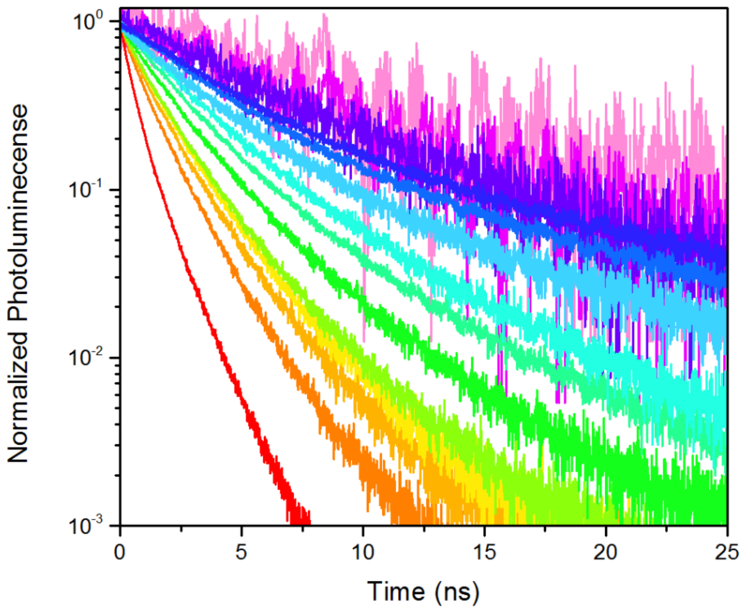

Fig. S7. Treated MoS$_2$ time-resolved luminescence. Photoluminescence decay spectrum measured over a pump-fluence dynamic range of 5×10^{-4} μJ cm^{-2} to 20 μJ cm^{-2}.

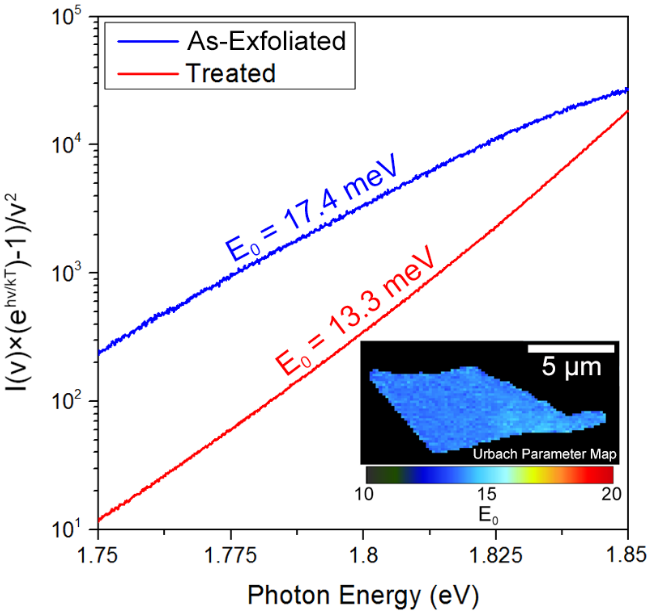

Fig. S8. Band-edge Sharpness. Band edge tails extracted from the PL spectrum using the van Roosbroeck-Shockley equation, showing the improvement of the Urbach parameter; the insert shows a spatial map of the Urbach parameter for a TFSI treated sample.

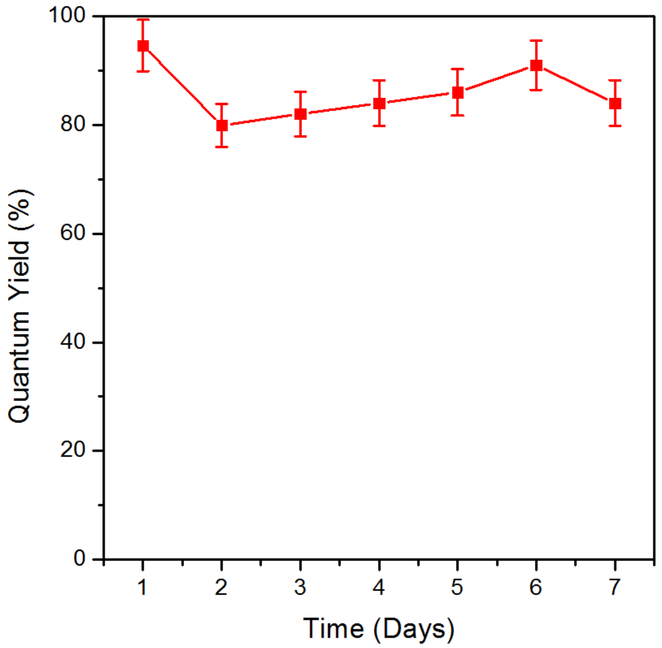

Fig. S9. Treatment Stability. QY measured at an incident power of 5×10^{-3} W cm^{-2} over one week; the sample was stored in ambient conditions (20° to 22°C, 40 to 60% relative humidity).

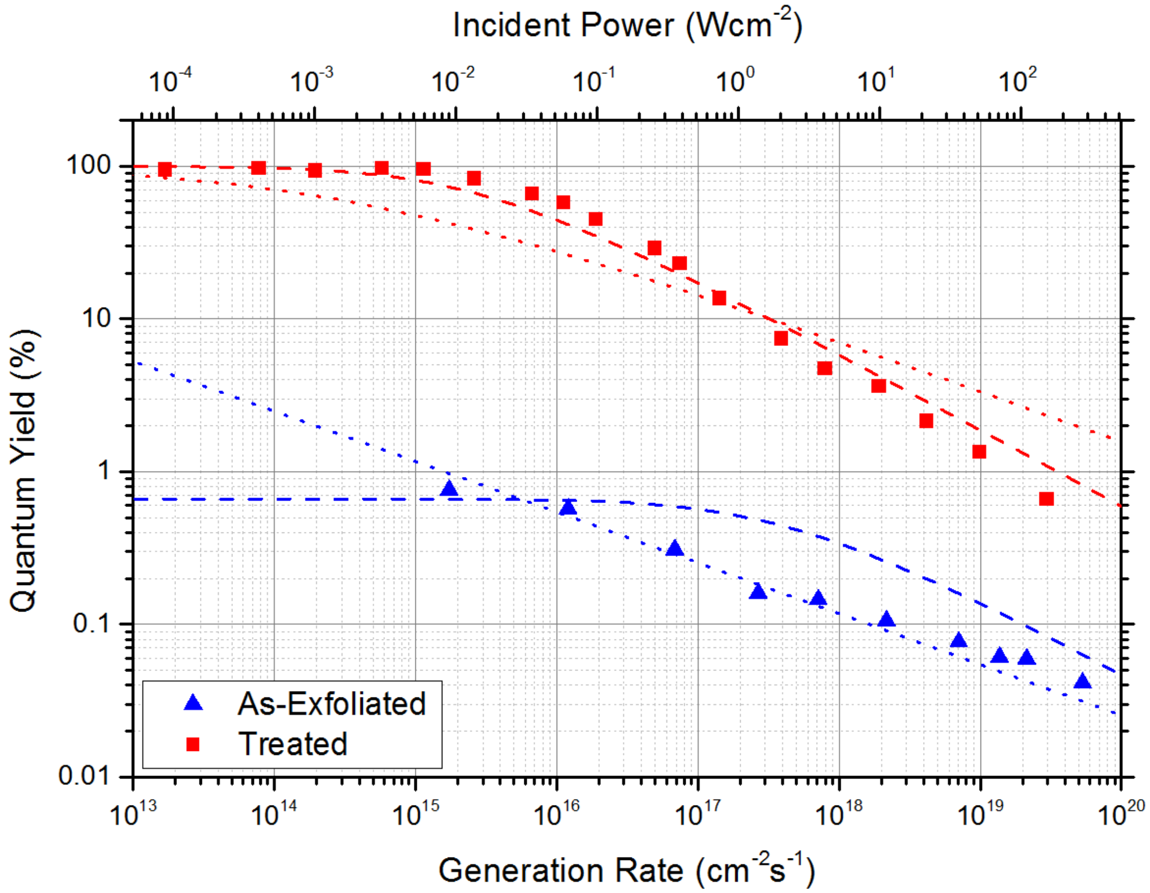

Fig. S10. Recombination Model. Pump-power dependence of the QY for as-exfoliated and treated MoS_2. Dotted curves show the standard semiconductor recombination model while the dashed curves show the modified recombination model for an excitonic system.

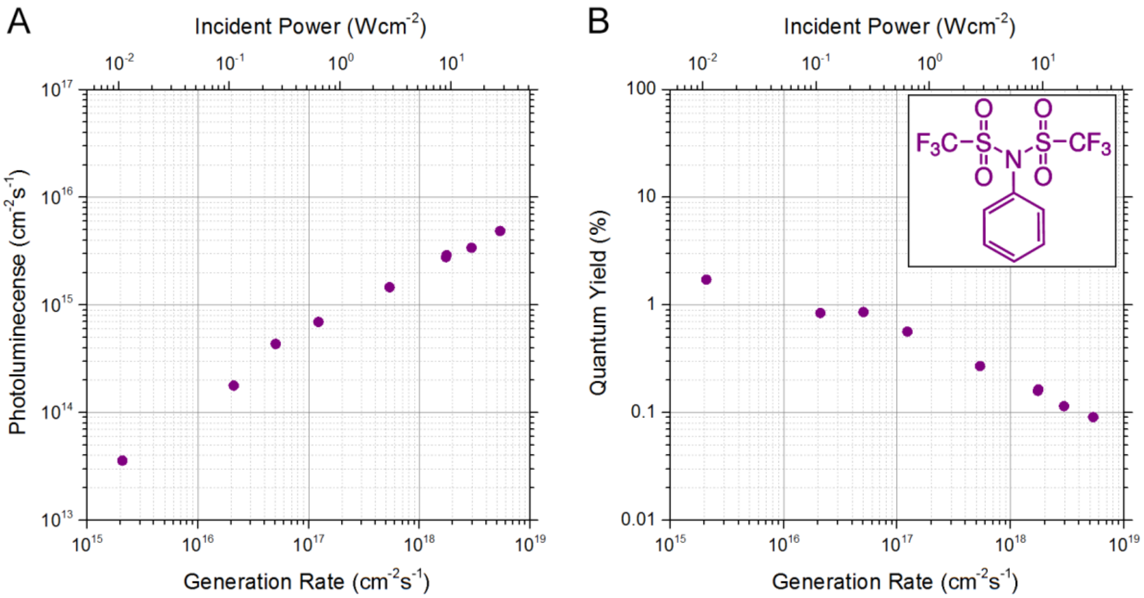

Fig. S11. Luminescence yield after treatment in Ph-TFSI. (**A**) Pump-power dependence of the integrated luminescence of MoS_2 treated by Ph-TFSI in DCB/DCE (9/1 v/v%). (**B**) Pump-power dependence of the QY for MoS_2 treated by Ph-TFSI in DCB/DCE (9/1 v/v%).

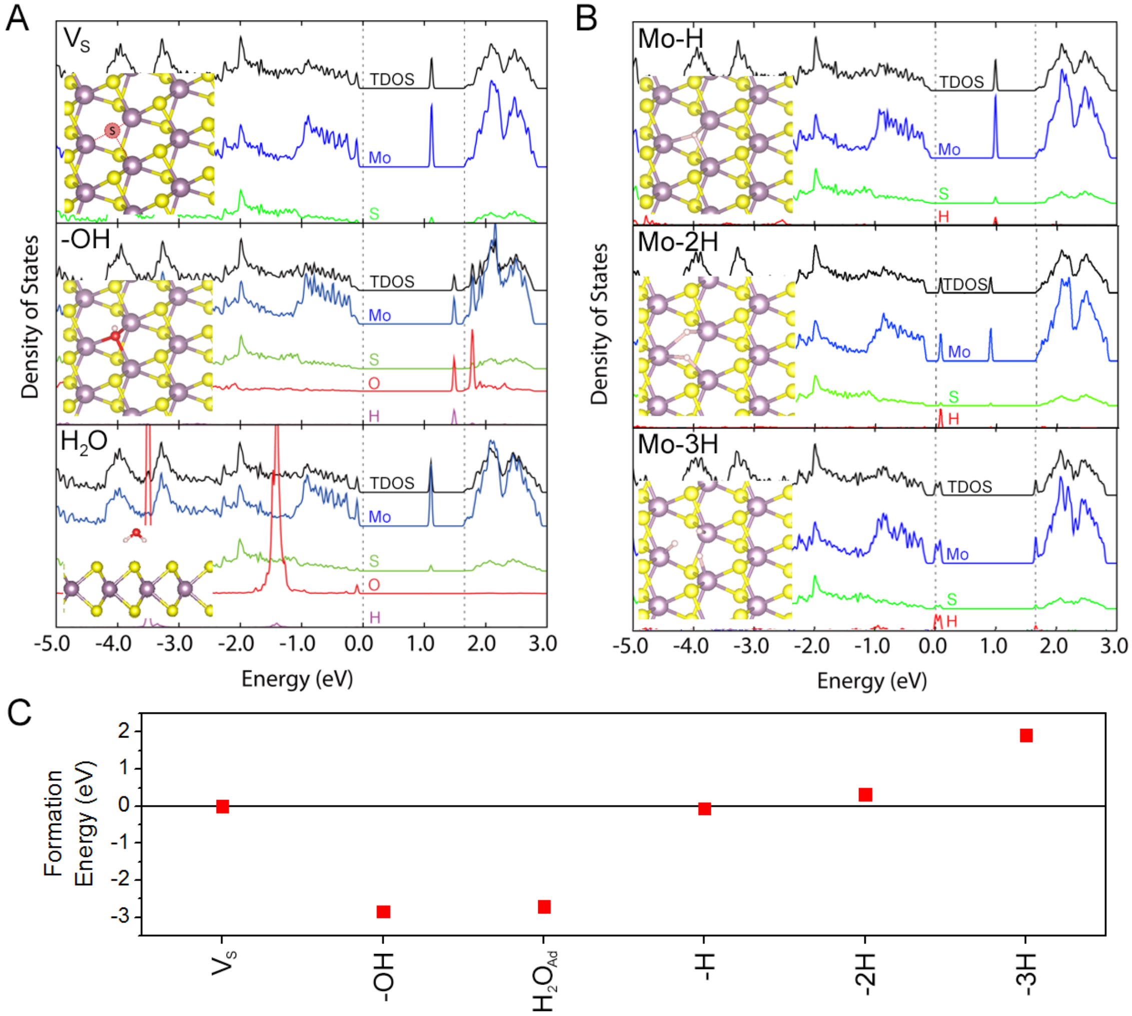

Fig. S12. DoS and formation energy calculations for possible defect/passivation configurations. (**A**) Calculated DoS for sulfur vacancies (V_s), adsorbed –OH at the V_s site, and adsorbed water. (**B**) Calculated DoS for a sulfur vacancy site passivated by one, two, or three hydrogen atoms. (**C**) Energy of formation for the chemical configurations shown in (**A**) and (**B**).

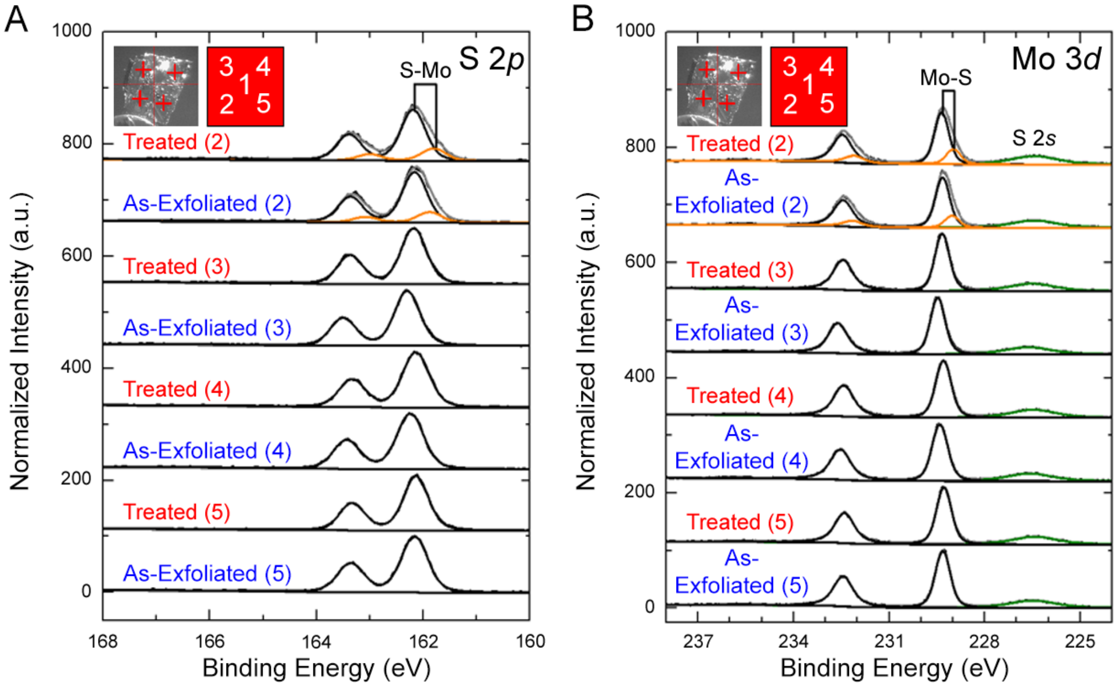

Fig. S13. XPS spatial analysis. (**A**) S *2p* core levels for the same MoS_2 flake before and after treatment measured at four different spots; spectra for the center is shown in Fig. 4E. (**B**) Mo *3d* core levels for the same MoS_2 flake before and after treatment measured at four different spots; spectra for the center is shown in Fig. 4E.

Table S1. Summary of the effect of various treatment on the QY. Quantum yield measured at a fixed illumination intensity of 2×10^{-2} W cm^{-2} after immersion in the target molecule for 15 minutes. As-exfoliated MoS_2 has a QY of 0.64±0.04% at 2×10^{-2} W cm^{-2}.

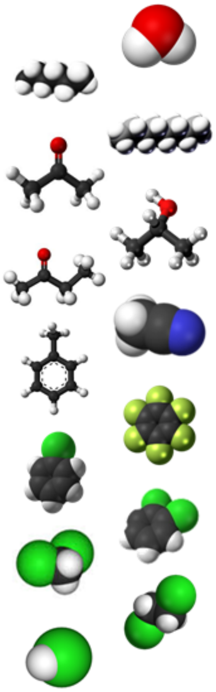

Treatment	**Chemical formula**	**QY at $2\text{x}10^{-2}$ W/cm^2**
Pristine MoS_2	MoS_2	0.6%
Water	H_2O	2.0%
Hexane	C_6H_{14}	0.7%
Decane	$C_{10}H_{22}$	0.4%
Acetone	C_3H_6O	0.8%
Isopropyl Alcohol	C_3H_8O	1.0%
Butanone	C_4H_8O	0.5%
Acetronitrile	CH_3CN	1.6%
Toluene	C_7H_8	0.6%
hexafluorobenzene	C_6F_6	1.2%
Chlorobenzene	C_6H_5Cl	1.7%
1 2-dichlorobenzene	$C_6H_4Cl_2$	8.7%
Dichloromethane	CH_2Cl_2	1.5%
1,2-Dichloroethane	$C_2H_4Cl_2$	7.0%
Hydrochloric acid	HCl	1.9%

Table S2. S/Mo Ratio. Error analysis of the sulfur to molybdenum ratio extracted from XPS data taken on the same locations (as indicated in Fig. S13) both before and after treatment by TFSI.

	Spot 1	*Spot 2*	*Spot 3*	*Spot 4*	*Spot 5*
As-Exfoliated	1.791±0.040	1.794±0.057	1.910±0.043	1.885±0.027	1.845±0.041
Treated	2.016±0.045	1.900±0.043	1.924±0.069	1.960±0.044	1.946±0.044

Author Contributions

M.A., D.-H.L., D.K., and A.J. designed the experiments. M.A. and J.W.A. designed and constructed the optical setups used in the measurements. M.A. and D.-H.L. performed the steady-state measurements. M.A., J.X., and D.-H.L. performed time-resolved measurements. D.K. designed and performed the various chemical treatments. A.A., R.A., and R.M.W performed XPS measurements and analysis of MoS_2 before and after TFSI treatments. J.N., S.KC, and K.C. performed DFT simulations. S.R.M. and D.H.L. prepared the MoS_2 samples. M.A., D.-H.L., J.W.A., E.Y., and A.J. analyzed the data. M.A., D.-H.L. D.K., and A.J. wrote the manuscript. All authors discussed the results and commented on the manuscript.

References and Notes

1. F. Xia, H. Wang, D. Xiao, M. Dubey, A. Ramasubramaniam, Two-dimensional material nanophotonics. *Nat. Photonics* **8**, 899–907 (2014). doi:10.1038/nphoton.2014.271

2. S. Wu, S. Buckley, J. R. Schaibley, L. Feng, J. Yan, D. G. Mandrus, F. Hatami, W. Yao, J. Vučković, A. Majumdar, X. Xu, Monolayer semiconductor nanocavity lasers with ultralow thresholds. *Nature* **520**, 69–72 (2015). Medline doi:10.1038/nature14290

3. H. Fang, C. Battaglia, C. Carraro, S. Nemsak, B. Ozdol, J. S. Kang, H. A. Bechtel, S. B. Desai, F. Kronast, A. A. Unal, G. Conti, C. Conlon, G. K. Palsson, M. C. Martin, A. M. Minor, C. S. Fadley, E. Yablonovitch, R. Maboudian, A. Javey, Strong interlayer coupling in van der Waals heterostructures built from single-layer chalcogenides. *Proc. Natl. Acad. Sci. U.S.A.* **111**, 6198–6202 (2014). Medline doi:10.1073/pnas.1405435111

4. L. Britnell, R. M. Ribeiro, A. Eckmann, R. Jalil, B. D. Belle, A. Mishchenko, Y.-J. Kim, R. V. Gorbachev, T. Georgiou, S. V. Morozov, A. N. Grigorenko, A. K. Geim, C. Casiraghi, A. H. Castro Neto, K. S. Novoselov, Strong light-matter interactions in heterostructures of atomically thin films. *Science* **340**, 1311–1314 (2013). Medline doi:10.1126/science.1235547

5. K. F. Mak, K. He, J. Shan, T. F. Heinz, Control of valley polarization in monolayer MoS_2 by optical helicity. *Nat. Nanotechnol.* **7**, 494–498 (2012). doi:10.1038/nnano.2012.96

6. S. B. Desai, G. Seol, J. S. Kang, H. Fang, C. Battaglia, R. Kapadia, J. W. Ager, J. Guo, A. Javey, Strain-induced indirect to direct bandgap transition in multilayer WSe_2. *Nano Lett.* **14**, 4592–4597 (2014). Medline doi:10.1021/nl501638a

7. S. Tongay, J. Suh, C. Ataca, W. Fan, A. Luce, J. S. Kang, J. Liu, C. Ko, R. Raghunathanan, J. Zhou, F. Ogletree, J. Li, J. C. Grossman, J. Wu, Defects activated photoluminescence in two-dimensional semiconductors: Interplay between bound, charged, and free excitons. *Sci. Rep.* **3**, 2657 (2013). Medline doi:10.1038/srep02657

8. A. Chernikov, T. C. Berkelbach, H. M. Hill, A. Rigosi, Y. Li, O. B. Aslan, D. R. Reichman, M. S. Hybertsen, T. F. Heinz, Exciton binding energy and nonhydrogenic Rydberg series in monolayer WS_2. *Phys. Rev. Lett.* **113**, 076802 (2014). Medline doi:10.1103/PhysRevLett.113.076802

9. H. M. Hill, A. F. Rigosi, C. Roquelet, A. Chernikov, T. C. Berkelbach, D. R. Reichman, M. S. Hybertsen, L. E. Brus, T. F. Heinz, Observation of excitonic Rydberg states in monolayer MoS_2 and WS_2 by photoluminescence excitation spectroscopy. *Nano Lett.* **15**, 2992–2997 (2015). Medline doi:10.1021/nl504868p

10. T. C. Berkelbach, M. S. Hybertsen, D. R. Reichman, Theory of neutral and charged excitons in monolayer transition metal dichalcogenides. *Phys. Rev. B* **88**, 045318 (2013). doi:10.1103/PhysRevB.88.045318

11. L. Yuan, L. Huang, Exciton dynamics and annihilation in WS_2 2D semiconductors. *Nanoscale* **7**, 7402–7408 (2015). Medline doi:10.1039/C5NR00383K

12. K. F. Mak, C. Lee, J. Hone, J. Shan, T. F. Heinz, Atomically thin MoS_2: A new direct-gap semiconductor. *Phys. Rev. Lett.* **105**, 136805 (2010). Medline doi:10.1103/PhysRevLett.105.136805

13. H. Wang, C. Zhang, F. Rana, Ultrafast dynamics of defect-assisted electron-hole recombination in monolayer MoS_2. *Nano Lett.* **15**, 339–345 (2015). Medline doi:10.1021/nl503636c

14. Materials and methods are available as supplementary materials on *Science* Online.

15. I. Schnitzer, E. Yablonovitch, C. Caneau, T. J. Gmitter, Ultrahigh spontaneous emission quantum efficiency, 99.7% internally and 72% externally, from AlGaAs/GaAs/AlGaAs double heterostructures. *Appl. Phys. Lett.* **62**, 131–133 (1993). doi:10.1063/1.109348

16. Y. S. Park, A. V. Malko, J. Vela, Y. Chen, Y. Ghosh, F. García-Santamaría, J. A. Hollingsworth, V. I. Klimov, H. Htoon, Near-unity quantum yields of biexciton emission from CdSe/CdS nanocrystals measured using single-particle spectroscopy. *Phys. Rev. Lett.* **106**, 187401 (2011). Medline doi:10.1103/PhysRevLett.106.187401

17. P. T. Landsberg, Non-radiative transitions in semiconductors. *Phys. Status Solidi* **41**, 457–489 (1970). doi:10.1002/pssb.19700410202

18. F. Wang, Y. Wu, M. S. Hybertsen, T. F. Heinz, Auger recombination of excitons in one-dimensional systems. *Phys. Rev. B* **73**, 245424 (2006). doi:10.1103/PhysRevB.73.245424

19. H. Wang, J. H. Strait, C. Zhang, W. Chan, C. Manolatou, S. Tiwari, F. Rana, Fast exciton annihilation by capture of electrons or holes by defects via Auger scattering in monolayer metal dichalcogenides. *Phys. Rev. B* **91**, 165411 (2015). doi:10.1103/PhysRevB.91.165411

20. C. Mai, A. Barrette, Y. Yu, Y. G. Semenov, K. W. Kim, L. Cao, K. Gundogdu, Many-body effects in valleytronics: Direct measurement of valley lifetimes in single-layer MoS_2. *Nano Lett.* **14**, 202–206 (2014). Medline doi:10.1021/nl403742j

21. T. Korn, S. Heydrich, M. Hirmer, J. Schmutzler, C. Schuller, Low-temperature photocarrier dynamics in monolayer MoS_2. *Appl. Phys. Lett.* **99**, 102109 (2011). doi:10.1063/1.3636402

22. A. Iribarren, R. Castro-Rodriguez, V. Sosa, J. L. Pena, Band-tail parameter modeling in semiconductor materials. *Phys. Rev. B* **58**, 1907–1911 (1998). doi:10.1103/PhysRevB.58.1907

23. Z. Liu, M. Amani, S. Najmaei, Q. Xu, X. Zou, W. Zhou, T. Yu, C. Qiu, A. G. Birdwell, F. J. Crowne, R. Vajtai, B. I. Yakobson, Z. Xia, M. Dubey, P. M. Ajayan, J. Lou, Strain and structure heterogeneity in MoS_2 atomic layers grown by chemical vapour deposition. *Nat. Commun.* **5**, 5246 (2014). Medline

24. A. Azcatl, S. McDonnell, S. K. C, X. Peng, H. Dong, X. Qin, R. Addou, G. I. Mordi, N. Lu, J. Kim, M. J. Kim, K. Cho, R. M. Wallace, MoS_2 functionalization for ultra-thin atomic layer deposited dielectrics. *Appl. Phys. Lett.* **104**, 111601 (2014). doi:10.1063/1.4869149

25. C. P. Lu, G. Li, J. Mao, L. M. Wang, E. Y. Andrei, Bandgap, mid-gap states, and gating effects in MoS_2. *Nano Lett.* **14**, 4628–4633 (2014). Medline doi:10.1021/nl501659n

26. S. McDonnell, R. Addou, C. Buie, R. M. Wallace, C. L. Hinkle, Defect-dominated doping and contact resistance in MoS_2. *ACS Nano* **8**, 2880–2888 (2014). Medline doi:10.1021/nn500044q

27. R. Addou, S. McDonnell, D. Barrera, Z. Guo, A. Azcatl, J. Wang, H. Zhu, C. L. Hinkle, M. Quevedo-Lopez, H. N. Alshareef, L. Colombo, J. W. Hsu, R. M. Wallace, Impurities and electronic property variations of natural MoS_2 crystal surfaces. *ACS Nano* **9**, 9124–9133 (2015). Medline doi:10.1021/acsnano.5b03309

28. R. Addou, L. Colombo, R. M. Wallace, Surface defects on natural MoS_2. *Appl. Mat. Interfaces.* **7**, 11921–11929 (2015). doi:10.1021/acsami.5b01778

29. J. Y. Noh, H. Kim, Y. S. Kim, Stability and electronic structures of native defects in single-layer MoS_2. *Phys. Rev. B* **89**, 205417 (2014). doi:10.1103/PhysRevB.89.205417

30. A. P. Nayak, S. Bhattacharyya, J. Zhu, J. Liu, X. Wu, T. Pandey, C. Jin, A. K. Singh, D. Akinwande, J. F. Lin, Pressure-induced semiconducting to metallic transition in multilayered molybdenum disulphide. *Nat. Commun.* **5**, 3731 (2014). Medline doi:10.1038/ncomms4731

31. M. Koppelman, Uncertainty analysis in photometric observations. *Proc. Soc. Astro. Sci.* **24**, 107–110 (2005).

32. H. Zeng, J. Dai, W. Yao, D. Xiao, X. Cui, Valley polarization in MoS_2 monolayers by optical pumping. *Nat. Nanotechnol.* **7**, 490–493 (2012). Medline doi:10.1038/nnano.2012.95

33. S. Wu, S. Buckley, A. M. Jones, J. S. Ross, N. J. Ghimire, J. Yan, D. G. Mandrus, W. Yao, F. Hatami, J. Vučković, A. Majumdar, X. Xu, Control of two-dimensional excitonic light emission via photonic crystal. *2D Mater.* **1**, 011001 (2014). doi:10.1088/2053-1583/1/1/011001

34. D. Magde, R. Wong, P. G. Seybold, Fluorescence quantum yields and their relation to lifetimes of rhodamine 6G and fluorescein in nine solvents: Improved absolute standards for quantum yields. *Photochem. Photobiol.* **75**, 327–334 (2002). Medline doi:10.1562/0031-8655(2002)075<0327:FQYATR>2.0.CO;2

35. E. Yablonovitch, G. D. Cody, Intensity enhancement in textured optical sheets for solar cells. *IEEE Trans. Electron. Dev.* **29**, 300–305 (1982). doi:10.1109/T-ED.1982.20700

36. E. Yablonovitch, T. J. Gmitter, R. Bhat, Inhibited and enhanced spontaneous emission from optically thin AlGaAs/GaAs double heterostructures. *Phys. Rev. Lett.* **61**, 2546–2549 (1988). Medline doi:10.1103/PhysRevLett.61.2546

37. W. F. Krupke, Induced-emission cross sections in neodymium laser glasses. *IEEE J. Quantum Electron.* **10**, 450–457 (1974). doi:10.1109/JQE.1974.1068162

38. P. Hohenberg, W. Kohn, Inhomogeneous electron gas. *Phys. Rev.* **136**, B864–B871 (1964). doi:10.1103/PhysRev.136.B864

39. W. Kohn, L. Sham, Self-consistent equations including exchange and correlation effects. *J. Phys. Rev.* **140**, A1133–A1138 (1965). doi:10.1103/PhysRev.140.A1133

40. P. E. Blöchl, Projector augmented-wave method. *Phys. Rev. B* **50**, 17953–17979 (1994). doi:10.1103/PhysRevB.50.17953

41. G. Kresse, D. Joubert, From ultrasoft pseudopotentials to the projector augmented-wave method. *Phys. Rev. B* **59**, 1758–1775 (1999). doi:10.1103/PhysRevB.59.1758

42. G. Kresse, J. Furthmüller, Efficiency of ab-initio total energy calculations for metals and semiconductors using a plane-wave basis set. *Comput. Mater. Sci.* **6**, 15–50 (1996). doi:10.1016/0927-0256(96)00008-0

43. G. Kresse, J. Furthmüller, Efficient iterative schemes for ab initio total-energy calculations using a plane-wave basis set. *Phys. Rev. B* **54**, 11169–11186 (1996). doi:10.1103/PhysRevB.54.11169

44. S. L. Chuang, *Physics of Photonic Devices* (Wiley, Hoboken, NJ, ed. 2, 2009).

45. L. Yang, K. Majumdar, H. Liu, Y. Du, H. Wu, M. Hatzistergos, P. Y. Hung, R. Tieckelmann, W. Tsai, C. Hobbs, P. D. Ye, Chloride molecular doping technique on 2D materials: WS_2 and MoS_2. *Nano Lett.* **14**, 6275–6280 (2014). Medline doi:10.1021/nl502603d

46. H. Qiu, T. Xu, Z. Wang, W. Ren, H. Nan, Z. Ni, Q. Chen, S. Yuan, F. Miao, F. Song, G. Long, Y. Shi, L. Sun, J. Wang, X. Wang, Hopping transport through defect-induced localized states in molybdenum disulphide. *Nat. Commun.* **4**, 2642 (2013). Medline doi:10.1038/ncomms3642

47. Y. Cai, Z. Bai, H. Pan, Y. P. Feng, B. I. Yakobson, Y. W. Zhang, Constructing metallic nanoroads on a MoS_2 monolayer via hydrogenation. *Nanoscale* **6**, 1691–1697 (2014). Medline doi:10.1039/C3NR05218D

48. C. J. Wright, C. Sampson, D. Fraser, R. B. Moyes, P. B. Wells, C. Riekel, Hydrogen sorption by molybdenum sulphide catalysts. *J. Chem. Soc. Faraday Trans. I* **76**, 1585–1598 (1980). doi:10.1039/f19807601585